

Microwave spectrum of square permalloy dots: Multidomain state

M. Bailleul,^{1,2,3,*} R. Höllinger,² K. Perzlmaier,² and C. Fermon³

¹*Institut de Physique et Chimie des Matériaux de Strasbourg, UMR 7504 ULP-CNRS, 23 rue du Loess BP 43, 67034 Strasbourg Cedex 2, France*

²*Institut für Experimentelle und Angewandte Physik, Universität Regensburg, 93040 Regensburg, Germany*

³*Service de Physique de l'État Condensé, DRECAM/DSM CEA Saclay, Orme des Merisiers, 91191 Gif sur Yvette, France*

(Received 23 April 2007; revised manuscript received 27 September 2007; published 3 December 2007)

We provide in this paper a detailed interpretation of the measured and simulated spin-wave spectra for Permalloy square dots in a Landau remanent configuration. Various semianalytical approaches are combined to show how the domain walls present in the Landau configuration may (i) confine low-frequency spin waves and (ii) set a triangular geometry for the propagation of higher frequency spin waves, which leads to a somehow counterintuitive quantization process. The knowledge gained from this study is finally used to reconstruct the magnetization process of the dots from the evolution of their microwave spectrum under an applied field.

DOI: [10.1103/PhysRevB.76.224401](https://doi.org/10.1103/PhysRevB.76.224401)

PACS number(s): 75.30.Ds, 76.50.+g, 75.60.Ch

I. INTRODUCTION

The normal modes of the magnetization field in micrometer size elements (spin-wave modes) have been extensively studied for a few years.¹ The motivations for this are not only technological (high speed magnetic devices for data processing, recording, and sensing) but also fundamental. Indeed, on the micrometer scale, the dynamics of the magnetization field involves a quite subtle interplay between the exchange and dipolar interactions. This results in several properties contrary to the intuition derived from conventional wave mechanics (waves with nonmonotonic dispersion² and breakdown of Chladni's law³).

Up to now, the efforts in the field of dynamic micromagnetism have been concentrated on a few types of magnetic ground states: rectangular elements in a quasisaturated state (see, e.g., Ref. 4 and references therein) or elliptical elements in a quasisaturated or vortex state (see, e.g., Refs. 5–8 and references therein). In these cases, the observed normal modes could be successfully interpreted in terms of quantized and localized modes with an additional low-frequency mode associated with the motion of a vortex. However, several complications are expected when the magnetic ground state comprises domain walls. Those strongly localized features are indeed expected to confine and/or to scatter spin waves.^{9,10} This was confirmed by recent experiments,^{11–18} where the normal modes have been imaged for the Landau configuration.¹⁹ In addition to a vortex-motion mode, these measurements revealed a mode strongly confined in the domain walls and several spin-wave mode features extending in the domains, the shape of which indicates a sizable influence of the domain walls. With the help of numeric simulations,^{20–24} those features were qualitatively reproduced and the normal modes were classified according to their symmetry properties. However, a physical understanding of both domain-wall modes and domain modes is still missing. This paper aims at providing such a description.

For this purpose, we make use of a microwave absorption spectrum measured for an assembly of Permalloy square dots in its remanent state. We first show that this spectrum is well reproduced by a full micromagnetic simulation for a square

dot in the Landau configuration. In a second time, we propose a set of semianalytical calculations accounting for the domain-wall modes and domain mode features observed in the measured and simulated spectra. Note that most of the experimental, numerical, and theoretical approaches are identical to those described in Ref. 4, where the same Permalloy square dots were brought in the quasisaturated state by applying a high enough magnetic field (10–150 mT). In this respect, the present paper constitutes, therefore, the low field counterpart of Ref. 4.

The paper is organized as follows. The experimental method is first described in Sec. II. The measured absorption peaks are then reproduced and identified with the help of a micromagnetic simulation (Sec. III). Sections IV–VI are devoted to the understanding of these features: While the low-frequency peaks are described within a simple domain-wall resonance framework (Sec. IV), the high-frequency features are attributed to a more complex spin-wave quantization process, which is analyzed in detail for the simpler case of an “isolated domain” (Sec. V). For the case of the Landau configuration, we show how the symmetry influences this process (Sec. VI). Our description of domain and domain-wall modes is finally applied to the interpretation of the evolution of the microwave spectrum under the application of a small magnetic field (Sec. VII). A quite general discussion of the notion of “regularity” for spin-wave spectra is provided in the Appendix.

II. EXPERIMENTAL SETUP

As in Ref. 4, the system investigated is a row of 103 Permalloy square dots having a side $w=3\ \mu\text{m}$, a thickness $t=30\ \text{nm}$, and spaced $3\ \mu\text{m}$ from each other. At remanence, most of these dots exhibit a Landau configuration [see a typical magnetic force microscopy picture in Fig. 1(b)]. Their microwave spectrum is measured with the help of a frequency-domain broadband inductive technique. This experiment, which is described in detail in Ref. 4, may be summarized as follows: a shorted portion of a coplanar waveguide is fabricated on top of the row of dots [see a microphotograph of a small portion of the sample in Fig.

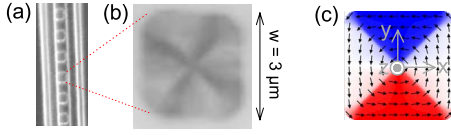


FIG. 1. (Color online) (a) Dark field microphotograph showing a small portion of the sample with the coplanar waveguide on top of the row of square dots. (b) Magnetic force microscope picture of one square dot at remanence. (c) Simulated Landau equilibrium configuration (note that the corners have been rounded with a 300 nm radius of curvature to reproduce the shape of the dots).

1(a)]. Using a vector network analyzer, we measure the self-inductance L of the coplanar waveguide loaded by the dots. A high field reference measurement is then subtracted from these data to get the variation of the self-inductance ΔL . This is a purely magnetic response function and the spin-wave modes appear as resonance peaks in its imaginary part $\Delta L''$.

The top curve in Fig. 2(a) shows a semilogarithmic plot of the spectrum measured at remanence.²⁵ The absorption appears to be somehow spread over seven broad peaks covering the range 1–8 GHz [see the black triangles in Fig. 2(a)]. As a first observation, notice how different this spectrum is from the one measured in the quasisaturated state, for which the absorption was concentrated into several narrow peaks [see Fig. 3 of Ref. 4 or Fig. 10(a) of the present paper]. This essential difference shall later be attributed to some “scattering” of the spin-wave modes by the domain walls (Sec. V). However, for the moment, let us simply reproduce this spectrum with the help of a micromagnetic simulation.

III. MICROMAGNETIC SIMULATION

As in Ref. 4, the simulation is performed in the time domain using the LLG code.²⁶ The dot is first discretized into 10 nm square cells and the Landau state is obtained by relaxation from an artificial four domain configuration [see Fig. 1(c), where the simulated equilibrium is shown together with the coordinate axes used in the remainder of this paper]. A 50 ps x -directed 1 mT square field pulse is then applied. The subsequent precession of the magnetization is registered within each cell and finally Fourier transformed to get the magnetic susceptibility χ_{xx} . The global absorption (i.e., the imaginary part of the spatial average of χ_{xx}) is displayed as the bottom curve in Fig. 2(a). One clearly distinguishes eight broad absorption peaks on this curve [see the blue triangles in Fig. 2(a)]. Most simulated peaks account correctly for the measured ones: the identification of the four peaks below 5.5 GHz and of the broad feature around the 7 GHz one is sketched by dashed lines in Fig. 2(a). On the other hand, the peaks simulated above 8 GHz do not show up in the measurement (probably because their intensity is too low). Note also that the 6 and 7.8 GHz measured peaks do not show up in the simulation at all. This should be understood in terms of the symmetry of the excitation field: The simulation uses a spatially uniform pulse field. Being perfectly symmetric with respect to the yz midplane of the microsquare, this excitation couples only to modes whose oscillating magnetization m_x is

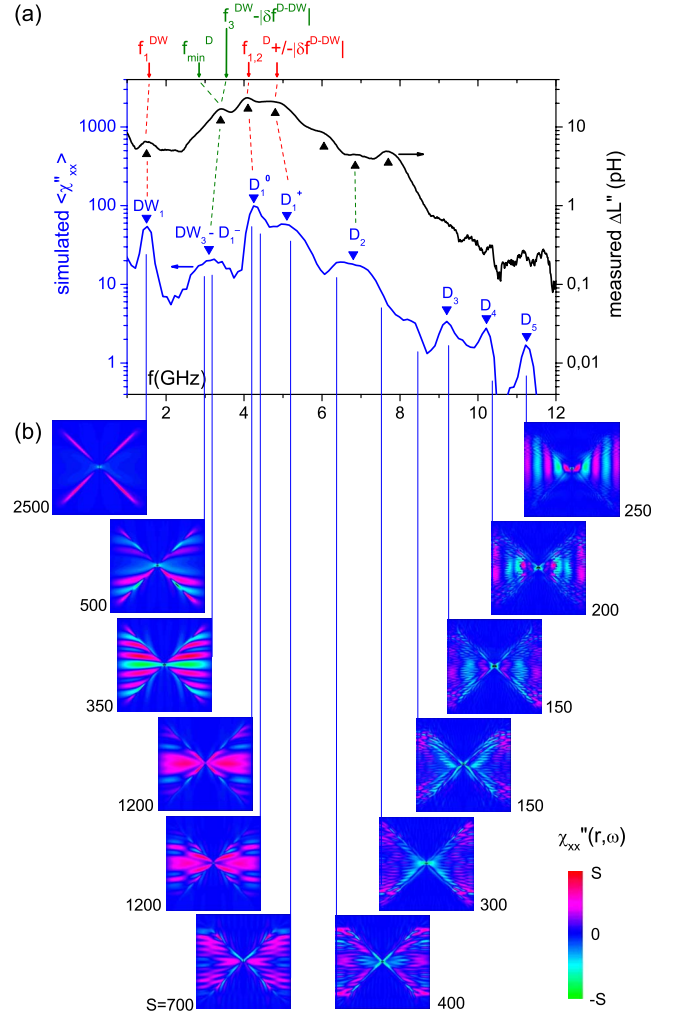


FIG. 2. (Color online) (a) Comparison between the measured (top curve, black) and the simulated (bottom curve, blue) micro-wave spectra. The peaks are named using a convention explained in the text. The arrows above the graph show the frequencies calculated using the semianalytical approaches of Secs. IV–VI. (b) Simulated susceptibility maps for 12 selected frequencies. The amplitude S spanned by the color scale is indicated for each map. The saturation magnetization, exchange constant, gyromagnetic ratio, and damping constant for the simulation are respectively $\mu_0 M_s = 1.13$ T, $A = 10^{-11}$ J m⁻¹, $\frac{\gamma}{2\pi} = 28$ GHz T⁻¹, and $\alpha = 0.005$.

symmetric with respect to the yz midplane. On the other hand, due to a small misalignment of the coplanar waveguide relative to the row of dots, the microwave field in the experiment is not perfectly symmetric and, therefore, slightly couples to modes with an antisymmetric m_x . This explanation is supported by a measurement on a sample providing a mostly antisymmetric excitation (DR sample in Ref. 4), which shows a significant enhancement of the 6 and 7.8 GHz peaks compared to the other ones (not shown).

Let us now identify the absorption peaks. For this purpose, susceptibility maps have been extracted from the simulation for several chosen frequencies [see Fig. 2(b)]. Note that only y oriented domains may contribute to χ_{xx} , which explains why the intensity is concentrated in the left and

right domains.²⁷ Note also the distinct change of the susceptibility map when going from one side of the peaks to the other (compare, e.g., the 3 and 3.1 GHz maps or the 4.1 and 4.2 GHz ones). This change is actually observed for all peaks except the 1.5 GHz one. Anticipating on the results of Sec. V, this is attributed to the composite nature of these peaks: the spectrum calculated in Sec. V is, indeed, composed of many modes whose frequency spacing is of the order of their intrinsic linewidth (about 125 MHz for in-plane magnetized Permalloy with $\alpha=0.005$). The susceptibility of these modes add together to form the total susceptibility shown in Fig. 2.²⁸ As a consequence, the labeling proposed below should be understood as a peak labeling, but not as a mode labeling.

Starting at the lowest frequency, the first peak appears to be strongly localized in the domain walls (DW's). Because it has only one antinode along each of them, it is labeled DW_1 . The map corresponding to the low-frequency part of the second peak also has maximum intensity in the domain walls. Because one recognizes in this map three antinodes along each domain wall, it will be referred to as DW_3 . All other susceptibility maps show significant intensity over the whole left and right domains (D 's). The corresponding peaks are, therefore, named D_n , where n describes the degree of inhomogeneity inside one domain. Following previous works on quantized spin waves, we know that the dispersion of spin waves is much stronger in the direction perpendicular to the equilibrium magnetization.^{2,29} So n is chosen as the number of nodal domains counted perpendicular to the magnetization of the domains considered (in other words, $n-1$ is the number of y -directed nodal lines). There are actually three peaks of the D_1 type. The susceptibility map for the lowest frequency one (named D_1^-) shows about ten x -directed nodal lines, while the maps for the two other ones (D_1^0 and D_1^+) are quite uniform. This frequency ordering is again explained in terms of spin-wave quantization: indeed, spin waves propagating parallel to the magnetization are known to have a slightly negative dispersion.^{2,29}

The aim of Secs. IV–VI is now to interpret these absorption features in detail. Our attention shall be concentrated onto the four lowest frequency peaks, which are also the most intense ones. For these peaks, the simulated and measured maxima do not differ by more than 300 MHz. In the following, the labels DW_1 , $DW_3-D_1^-$, D_1^0 , and D_1^+ shall, therefore, refer indiscriminately to measured and simulated peaks. We shall strive toward a physical description, which, though approximate, should be accurate enough to account quantitatively for the frequencies of these features. Moreover, we wish this description to account qualitatively for the broadness of most of these features and for the appearance of the corresponding modes. Anticipating the results of the next sections, the arrows on top of Fig. 2(a) show the frequencies obtained from our semianalytical calculations (in the following, the results of these calculations shall be noted $f_n^{D/DW}$). Notice the reasonable agreement with the position of the absorption peaks. Let us now start with a simple description of the specific dynamics of the domain walls.

IV. DOMAIN-WALL MODES

In order to describe the dynamics of the domain walls, one should first consider their equilibrium configuration. For

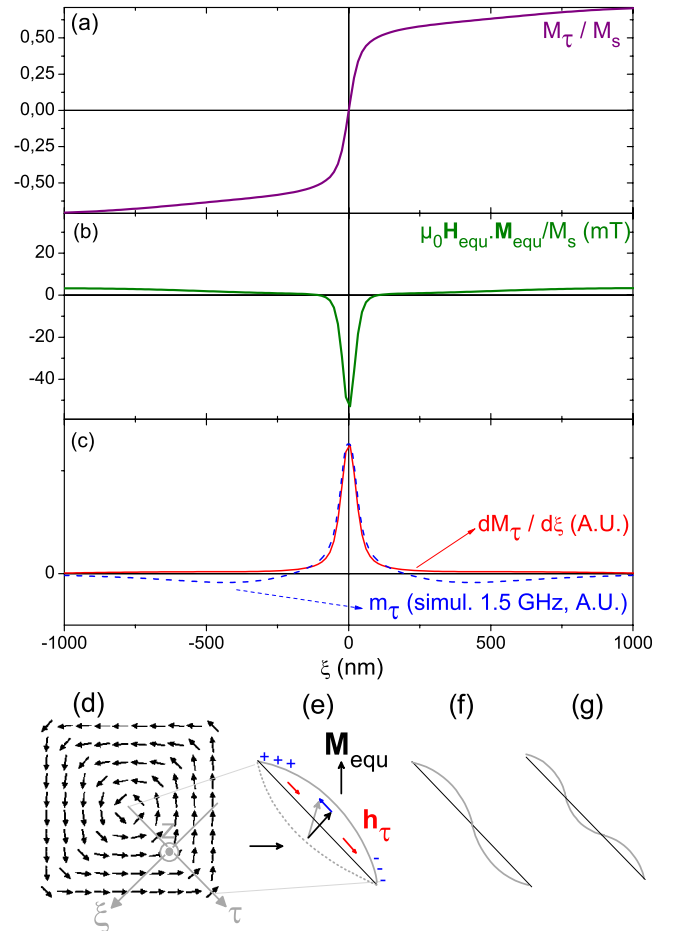


FIG. 3. (Color online) Profiles (a) of the equilibrium transverse magnetization and (b) of the equilibrium effective field across one domain wall. (c) Comparison of the oscillating magnetization profiles deduced from Eq. (1) (continuous line) and from the dynamical simulation (dotted line). (d) Definition of the system of coordinates. [(e)–(g)] Sketch of the bending of one domain wall for $n=1-3$. The distorted magnetization configuration is also sketched in (e), together with the induced magnetic charges and the corresponding in-plane dipole field h_τ .

this purpose, we define two axis ξ and τ directed respectively across and along one of the domain walls [see Fig. 3(d)], and we plot the simulated transverse equilibrium magnetization M_τ as a function of ξ [see Fig. 3(a)]. One recognizes from this plot the classical profile of a Néel wall:³⁰ a large part of the magnetization rotation is concentrated in a narrow core, while the remainder is distributed into two long tails. This picture is confirmed by inspecting the equilibrium effective field H_{equ} generated by this configuration [see Fig. 3(b)]. One recognizes a narrow dip in the core center and two shoulders in the tails, which are attributed respectively to the short-range and long-range parts of the dipole field generated by the core.³¹ Following recent works on edge modes,³² we expect the narrow dip to act as a potential well for the spin waves, thus creating modes highly localized in the domain-wall core. In the following, we shall proceed to a quantitative analysis of these modes. For this purpose, we will adapt to our geometry the theory of domain-wall resonance, which

was initially developed for bubble and stripe domains.^{33,34} This provides one with an ansatz for the dynamic magnetization, which we then inject into a variational calculation for estimating the mode frequencies.

As the core of the domain wall is much smaller than the dot, we first assume that the domain wall can move without a major change of its transverse magnetic configuration (which is the basic assumption of domain-wall resonance theory).^{33,34} The dynamic in-plane magnetization $\mathbf{m}(\xi, \tau)$ is, therefore, obtained by simply shifting the equilibrium wall configuration \mathbf{M} by a small amount $\epsilon(\tau)$:

$$\mathbf{m}(\xi, \tau) = \mathbf{M}(\xi + \epsilon(\tau), \tau) - \mathbf{M}(\xi, \tau) \approx \epsilon(\tau) \frac{\partial \mathbf{M}}{\partial \xi}(\xi, \tau). \quad (1)$$

This conjecture is confirmed by extracting $\frac{\partial M_x}{\partial \xi}$ from the equilibrium simulation and comparing it to a ξ cut of the 1.5 GHz simulated mode [see Fig. 3(c)]. Both profiles look very similar and fit quite well to a $\delta_{DW}=60$ nm wide Lorentzian.

We also assume the wall bending $\epsilon(\tau)$ to have a sinusoidal profile and to be pinned both at the corner and at the vortex,³⁵ with a given number of antinodes n in between [see Figs. 3(e)–3(g)]. This allows one to write the following ansatz for the in-plane dynamic magnetization:

$$m_{\tau,n}(\xi, \tau) = m_0 \frac{1}{4\xi^2 + \delta_{DW}^2} \sin\left(\frac{n\pi\tau}{l_{DW}} - \frac{n\pi}{2}\right). \quad (2)$$

Here, δ_{DW} and $l_{DW} = \frac{w}{2}$ stand respectively for the width and the length of one domain wall.

Let us now inspect the effective fields created by this quasistatic motion of the domain-wall core. Because the short scale structure of the domain wall is preserved, there are no extra in-plane dipole-exchange fields generated on the short scale. It is actually the bending of the domain wall which generates a nonzero in-plane effective field. As this deformation happens on quite a large length scale, this effective field is dominated by a long-range demagnetizing effect which occurs as follows: when it bends, the domain wall generates extra volume magnetic charges close to its extremities. These charges generate, in turn, a small dipole field oriented along the domain wall [h_τ in Fig. 3(e)]. Then, the motion of the domain wall also creates a torque which slightly tilts the magnetization out of the film plane. This out-of-plane dynamic magnetization m_z generates an effective field h_z . For the length scales of our problem ($\Lambda \ll t < \delta_w$, where $\Lambda = \sqrt{\frac{2A}{\mu_0 M_s^2}} = 5$ nm is the exchange length), h_z is dominated by the large out-of-plane demagnetizing term and m_z is simply proportional to m_τ and out-of-phase with respect to it (see, e.g., Appendix A in Ref. 4).

In a mechanical analogy, h_τ and h_z are to be interpreted as a restoring force and an inertia, and their combination determines the mode frequency.^{4,33,34} This picture is made quantitative using a variational approach:^{36–38} we calculate the effective demagnetizing factors $\langle G_{\alpha\alpha} \rangle$ by projecting the kernel of the dipolar interaction $G_{\alpha\beta}(\mathbf{r}, \mathbf{r}') = -\frac{\partial^2}{\partial x_\alpha \partial x_\beta} \frac{1}{|\mathbf{r} - \mathbf{r}'|}$ onto the ansatz³⁷ \mathbf{m}_n :

$$\langle G_{\alpha\alpha} \rangle_n = \frac{\int d\mathbf{r} \int d\mathbf{r}' m_{\alpha,n}(\mathbf{r}) G_{\alpha\alpha}(\mathbf{r} - \mathbf{r}') \bar{m}_{\alpha,n}(\mathbf{r}')}{\int d\mathbf{r} m_{\alpha,n}(\mathbf{r}) \bar{m}_{\alpha,n}(\mathbf{r})}, \quad (3)$$

and the mode frequencies are obtained with the help of a Kittel-like formula:

$$f_n^{DW} = \frac{|\gamma|}{2\pi} \mu_0 M_s \sqrt{\langle G_{\tau\tau} \rangle_n \langle G_{zz} \rangle_n}. \quad (4)$$

This calculation was done numerically by discretizing a 300 nm wide area around the domain wall into 60×60 parallelepipedic cells. We obtain in this way $f_1^{DW} = 1.6$ GHz, $f_2^{DW} = 2.9$ GHz, and $f_3^{DW} = 4.0$ GHz. Looking back at Fig. 2(a), we see that f_1^{DW} accounts perfectly for the DW_1 peak. On the other hand, because of its antisymmetric profile, the $n=2$ mode is not selected by a uniform excitation and, therefore, it does not show up in the susceptibility maps of Fig. 2(b). Finally, our calculated f_3^{DW} falls 1 GHz above the $DW_3-D_1^-$ peak. This discrepancy shall be interpreted in Sec. VI as a consequence of the dynamical coupling between this domain-wall mode and the set of domain modes: by accounting perturbatively for this coupling, we shall obtain a frequency $f_3^{DW} - |\delta f^{D-DW}| = 3.6$ GHz, in better agreement with the position of the $DW_3-D_1^-$ peak. Once we have seen how a domain wall generates its own vibration modes,³⁹ let us now see how the dynamics of the remainder of the dot is affected by the presence of domain walls.

V. SPIN-WAVE MODES IN A SATURATED TRIANGULAR BODY

In the Landau state, the shape of each domain is a triangular one. In this section, we consider, therefore, a fictitious preliminary problem consisting of the determination of the quantized spin-wave modes for a saturated and isolated triangular body. We shall later see how the domain modes in the Landau configuration might be connected to the spin-wave modes of such an “isolated” domain (Sec. VI). We start with a full numerical diagonalization of the eigensystem (Sec. V A). The high irregularity of the obtained spectrum indicates that this preliminary problem is already far from simple (see the Appendix for an interpretation of this lack of regularity). As a consequence, we shall give up trying to derive the frequencies and profiles of single modes. We shall rather describe the spectrum as a whole: On one hand, we shall predict generic properties such as the level spacing and the minimum frequency with the help of an approximate “adiabatical” quantization procedure (Sec. V B). On the other hand, we shall estimate the frequency for which the modes couple optimally to a uniform excitation (i.e., the frequency of the absorption maximum) with the help of a variational approach (Sec. V C).

A. Diagonalization

The body representing the right domain of the Landau configuration is shown in the inset of Fig. 4: it is an isorect-

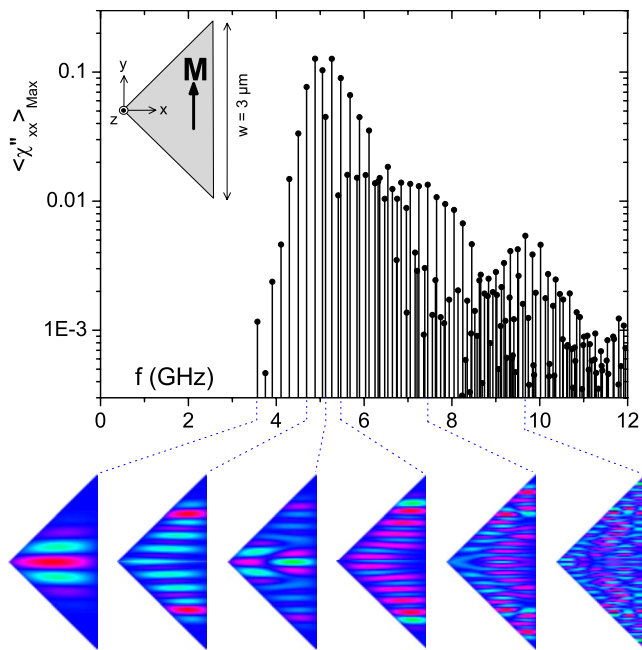


FIG. 4. (Color online) Spin-wave spectrum for the fictitious saturated triangular body problem (geometry shown in the inset). The eigenfrequency and eigenmodes were obtained by a diagonalization of the dynamical matrix. The maximum level of the spatially averaged susceptibility is reported for each mode as a vertical bar. Susceptibility maps are also reported for six selected modes at the bottom of the graph.

angle triangle with base $w=3 \mu\text{m}$. Its equilibrium magnetization is assumed to be uniformly saturated along its base.⁴⁰ All the eigenmodes of this problem are calculated using a diagonalization procedure already described in Ref. 4: The triangular body is first discretized into 23 nm wide square cells. By linearizing the Landau-Lifschitz equation, writing it in the frequency domain, and discretizing it, one obtains an eigensystem.⁴¹ The system is then solved with the help of a Householder reduction and a QL algorithm.⁴² The coupling of the eigenmodes to a uniform excitation is finally estimated by calculating the maximum of the spatially averaged susceptibility corresponding to each of them [see Eq. (B9) of Ref. 4]. The obtained spectrum is shown in the main panel of Fig. 4. Note that only modes symmetric with respect to the mirroring across the horizontal midaxis of the dots have been considered because antisymmetric modes cannot couple to the uniform excitation. One sees immediately from Fig. 4 that the spectrum does not consist of individual well-resolved peaks but, rather, of a dense series of levels, starting at about 3.5 GHz, reaching a maximum susceptibility around 5 GHz, and with a mean level spacing of the order of 200 MHz. Inspecting the eigenmodes (see the maps at the bottom of Fig. 4) does not allow one to recognize a clear nodal structure. In particular, one cannot distinguish any quasiuniform mode: all modes (even the most intense ones) appear to be quite inhomogeneous in the y direction (i.e., parallel to the equilibrium magnetization).

Apparently, a finite size body of triangular shape fails in producing well-defined standing spin-wave features dominat-

ing the absorption spectrum, as observed in the case of rectangular or elliptical geometries (see, e.g., Refs. 4–6 and 8, and references therein). This counterintuitive lack of regularity is attributed to the interplay between the anisotropic-nonmonotonic character of the spin-wave dispersion and the low symmetry of the triangular shape. A detailed interpretation of this lack of regularity is provided in the Appendix, where an analogy with the classical motion and the wave motion in bounded bodies (“billiards”) is proposed, together with an experimental verification relying on the spectra for obliquely magnetized squares. Note that this lack of regularity is of practical importance for our present discussion: the mean-level spacing of Fig. 4 is of the same order as the intrinsic linewidth of the Permalloy film (125 MHz for $\alpha=0.005$), so that individual modes are expected to be resolved neither in a measurement nor in a realistic micromagnetic simulation including the damping. The spectrum shown in Fig. 4 can, therefore, be seen as a structured quasicontinuum, which we shall now describe with the help of simplified calculations.

B. Semiclassics

From the conclusions of the last section and from those of the Appendix, it is clear that there exists no quantization procedure able to describe all normal modes for our geometry. However, it is clear that the overall spectrum should reflect somehow the shape of the dispersion of the spin waves and the specific boundary conditions governing their reflection on the edges. For pedagogical purposes, we propose below an “adiabatical” quantization procedure which does not describe realistically all normal modes, but allows one to understand better the appearance of the spectrum.

Taking advantage of the anisotropy of the spin-wave dispersion,^{2,29} we consider separately the quantization along the x direction (i.e., perpendicular to the equilibrium magnetization). More precisely, we assume the x profile of the dynamic magnetization to be sinusoidal, with vanishing amplitude at the left and right edges and n_x antinodes in between [see the sketch of the $n_x=1$ profile in Fig. 5(a)]. This “strong pinning” assumption is expected to be realistic for the micrometer size considered here.⁴³ Now, the triangular shape makes the x quantization wave vector y dependent:

$$k_x(y) = n_x \frac{\pi}{w/2 - y}. \quad (5)$$

In order to see the effect of the other component of the wave vector k_y , we calculate local spin-wave dispersions $f(n_x, y, k_y)$ by injecting Eq. (5) in the two-dimensional dipole-exchange spin-wave dispersion.² The resulting dispersions are three-dimensionally displayed in Fig. 5(b) for various locations y between the center of the triangle and one apex (from front to bottom) and for two different antinode numbers (gray curves, $n_x=1$; brown curves, $n_x=3$). Those curves provide one with a semiclassical picture of the propagation of spin waves through this triangular body: keeping its frequency constant, a spin wave coming from the center of the triangle changes its k_y gradually (“adiabatically”) in order to compensate for the increase in k_x due to the coming to

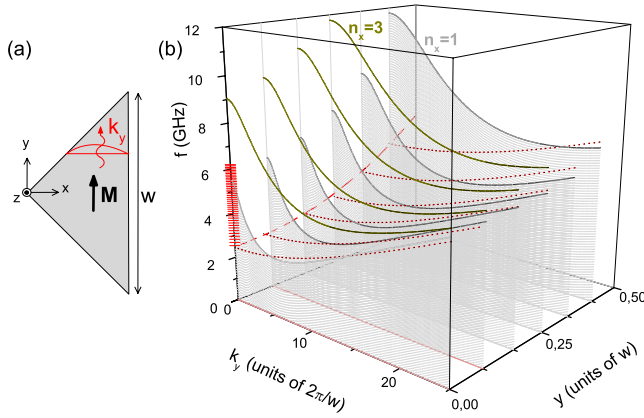


FIG. 5. (Color online) Semiclassical adiabatical description for spin waves propagating in a saturated triangular body. (a) Sketch for a spin-wave mode which is quantized along x (profile shown for $n_x=1$) and propagating along y . (b) Local dispersions $f(n_x, y, k_y)$ for $n_x=1$ (gray curves) and $n_x=3$ (brown curves). The red dotted curves are parabolic approximates of the local dispersions for $n_x=1$. The red dashed curve is a parabolic approximation of the minima of these dispersions. The eigenfrequencies calculated for the corresponding harmonic oscillator problem are reported as horizontal bars on the frequency axis.

gether of the two edges. The minimum frequency ($f_{min}=2.8$ GHz) is reached for an $n_x=1$ wave propagating from the center of the dot with $k_y^{min} \approx 7 \frac{2\pi}{w}$ (for which the $y=0$, $n_x=1$ dispersion has a minimum). This accounts correctly for the appearance of the lowest lying calculated eigenmode (3.5 GHz mode in Fig. 4). As one departs from the condition $y \approx 0$ and $k_y \approx k_y^{min}$, the frequency gradually increases (see, e.g., the 4.7 GHz mode in Fig. 4). The triangular shape may, therefore, be seen as a shallow potential well for each of the n_x^{th} partial wave.

To get a global picture of the resulting spectrum, we consider an oscillator problem which reproduces very roughly our wave-in-a-potential problem: We replace each local dispersion by a parabolic approximation [see dotted red curves in Fig. 5(b)] and we also fit the y dependence of the minima of these approximate dispersions to a parabola [see the dashed red curve in Fig. 5(b)]. The resulting approximate system (a wave with parabolic dispersion confined in a parabolic well) is exactly a harmonic oscillator. Solving for it, we obtain a series of levels with a nearly constant spacing of the order of 200 MHz [see the horizontal bars in Fig. 5(b)], in good agreement with the mean-level spacing seen in Fig. 4. This calculation illustrates directly the dependence of the spectrum on the size of the triangular body: decreasing the lateral size would increase the curvature of the potential well, resulting in an increase of the level spacing, which could allow one to resolve individual eigenmodes in a measurement or in a realistic micromagnetic simulation. Alternatively, decreasing the thickness would decrease the amplitude of the minimum of the local dispersions, resulting in a decrease of the number of short-wavelength low-frequency modes. The global appearance of the spectrum, is therefore, strongly size dependent. From our point of view, this is part of the explanation for the different aspects of the domain

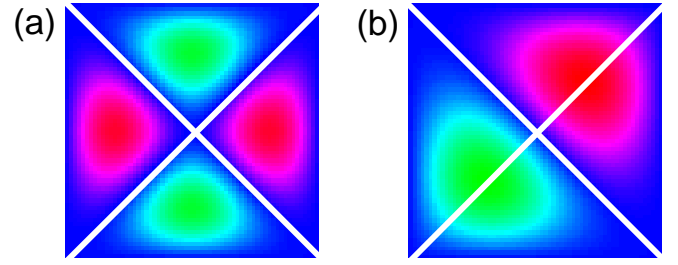


FIG. 6. (Color online) Ansatz for the oscillating magnetization of domain modes deduced from standing-wave modes for the full square. Equation (6) has been used with (a) $(p,q)=(1,3)$ and (b) $(p,q)=(1,2)$.

mode spectra reported in Ref. 14 (measurements on $0.75-4 \mu\text{m}$ wide, 16 nm thick squares), in Ref. 22 (simulation on a $1 \mu\text{m}$ wide, 16 nm thick square), in Ref. 21 (simulation on a 305 nm wide, 20 nm thick square), in Ref. 24 (simulation on a 150 nm wide, 25 nm thick square), and in the present paper (measurements and simulations on $3 \mu\text{m}$ wide, 30 nm thick squares).

Note that our adiabatical approximation does not allow the spin wave to switch between different n_x , which may happen as long as the frequency exceeds the minima of the corresponding dispersions. This happens actually for some of the modes (see, e.g., the 5.1 GHz map in Fig. 4). At higher frequencies, one even recognizes a “constant k_x ” behavior: as one goes from the dot center toward its top corner, the x spacing between nodal lines does not change much, but the number of nodal domains fitting between the two edges decreases gradually (see, e.g., the 9.5 GHz map in Fig. 4). These different behaviors illustrate again the difficulty to build a single rule for predicting the appearance of the spectrum.

The analysis reported above provides one with a global picture of the eigenmodes (what might be called the “spin-wave manifold” of the dot). However, it does not indicate which of these modes are likely to couple to the uniform excitation used in both the experiment and the simulation, i.e., it does not explain the position of the peak in Fig. 4. For this purpose, we shall now resort to a variational approach.

C. Variational estimate

Among the quasicontinuum described earlier, only modes having a sizable long-wavelength envelope may couple to a spatially uniform excitation. Naturally, the frequencies of these modes are governed by the shape of their envelope (more precisely, by the magnitude of the demagnetizing fields it generates) rather than by the short-wavelength details. We shall convert this idea into a quantitative estimate with the help of a variational approach: the ansatz for the envelope function is generated by subtracting from a standing-wave mode of the full square its image under the operation⁴⁴ $x \leftrightarrow y$:

$$m_{p,q}(x,y) = \cos\left(p\pi\frac{x}{w}\right)\cos\left(q\pi\frac{y}{w}\right) - \cos\left(q\pi\frac{x}{w}\right)\cos\left(p\pi\frac{y}{w}\right), \quad (6)$$

where $p \neq q$ are integers. The first two members of this family of functions (i.e., the most uniform ones) are shown in

TABLE I. Extended character table for the symmetry group C_{4v} . For the vectorial representation E , the matrices representing the symmetry operations are written for the basis (e_1, e_2) [instead of the equivalent basis (e_x, e_y) sketched in gray].




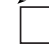


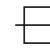
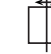
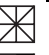



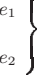
C_{4v}									
E	C_2	C_4^+	C_4^-	σ_1	σ_2	σ_x	σ_y		
	A_1	1	1	1	1	1	1	1	
	A_2	1	1	1	-1	-1	-1	-1	
	B_1	1	1	-1	-1	-1	1	1	
	B_2	1	1	-1	1	1	-1	-1	
	E	$\begin{pmatrix} 1 & 0 \\ 0 & 1 \end{pmatrix}$	$\begin{pmatrix} -1 & 0 \\ 0 & -1 \end{pmatrix}$	$\begin{pmatrix} 0 & -1 \\ 1 & 0 \end{pmatrix}$	$\begin{pmatrix} 0 & 1 \\ -1 & 0 \end{pmatrix}$	$\begin{pmatrix} 1 & 0 \\ 0 & -1 \end{pmatrix}$	$\begin{pmatrix} -1 & 0 \\ 0 & 1 \end{pmatrix}$	$\begin{pmatrix} 0 & 1 \\ 1 & 0 \end{pmatrix}$	$\begin{pmatrix} 0 & -1 \\ -1 & 0 \end{pmatrix}$

Fig. 6. Naturally, these functions all vanish along the first diagonal of the square ($y=x$), but they also vanish along the second diagonal for (p, q) both odds. While being as uniform as possible, the $(p, q)=(1, 3)$ function shown in Fig. 6(a) satisfies, therefore, strong-pinning boundary conditions at the edges of the triangle (these conditions are expected to be realistic for the micrometer size considered here).⁴³ This ansatz⁴⁵ is finally injected into a variational estimate of the frequency [see Eqs. (3) and (4) with $\tau=x$ and $\langle G_{zz} \rangle \approx 1$]:

$$f_{p,q}^T = \frac{|\gamma|}{2\pi} \mu_0 M_s \sqrt{\langle G_{xx} \rangle_{p,q}}. \quad (7)$$

The exchange interaction was neglected in writing Eq. (7), which is justified for the micrometer size considered here. This calculation is finally done numerically by discretizing the triangular body into 23 nm wide square cells, which gives $f_{1,3}^T = 5.0$ GHz, in good agreement with the frequency of the maximum of the spectrum in Fig. 4. On the other hand, the frequencies for higher-index ansatz, which all have nodal lines within the triangular domain [e.g., $(p, q)=(1, 5)$, not shown], are above 6 GHz, so that they might account for the low-intensity high-frequency shoulders observed in Fig. 4 around 7 and 9 GHz. Please note that such a procedure produces errors that are quadratic with respect to the difference between the ansatz and the true wave function. As a consequence, the ansatz is required to reproduce only very roughly the wave function. Let us now extend our analysis to the more complicated case of the full Landau configuration.

VI. DOMAIN MODES IN THE LANDAU CONFIGURATION

For a full description of quantized spin-wave modes in domains, it would be desirable to derive boundary conditions describing the behavior of the spin waves in the domain-wall regions. These boundary conditions should account both for the acceleration associated with the very low value of the equilibrium effective field in the core region [see Fig. 3(b)] and for the changes of wave vector allowed by conservation

laws (complicated reflection and/or refraction rules). This task is quite a nice challenge, but it is far beyond the scope of the present paper. However, an approximate description of the overall spectrum is still possible. This description proceeds in two steps: to justify the analogy with billiard systems (see the Appendix), it is enough to say that the spin waves undergo a pretty brutal change of wave vector when they meet a domain wall. The details of this change are not of major importance (there exist, indeed, billiard with Dirichlet, Neumann, or mixed boundary conditions). Once one accepts this analogy, it is likely that the domain spin-wave spectrum is nonregular (see the Appendix). Then, following Sec. V C, the main absorption peaks constituting this nonregular spectrum can be determined by describing the envelope of the modes which couple efficiently to the excitation. In the following, we show how to derive the behavior of this envelope from an analysis of the overall symmetry and of the dipole fields generated in the domain-wall regions. This analysis provides a simple ansatz, which can then be used for variational estimates of the peak frequencies.

The Landau configuration has the full symmetry of the square dot. As underlined by Yan *et al.*,²¹ group theory can be used to derive the possible symmetries for the eigenmodes. Table I summarizes the group theoretical description of the symmetry of the Landau configuration. This extended character table can be described as follows:⁴⁶ The group, labeled C_{4v} , consists of the eight symmetry operations sketched in the top row.⁴⁷ It admits five irreducible representations (four scalar ones and a vectorial one), which are listed in the left column. Eigenmodes belonging to these representations transform under the symmetry operation as indicated in the table. Pictorially, the mode profile (m_ϕ, m_z) in the whole square may be deduced from that in one elementary white triangle by unfolding it according to the symmetry operation, with an additional change of sign for dark triangles (see the sketches on the left of Table I). Quite naturally, the frequency and the appearance of normal modes are expected to depend quite critically on their symmetry, i.e., on the irreducible representation they belong to. The domains are, indeed, strongly coupled by dynamic dipole fields whose amplitude and orientation depend on the phase shift between

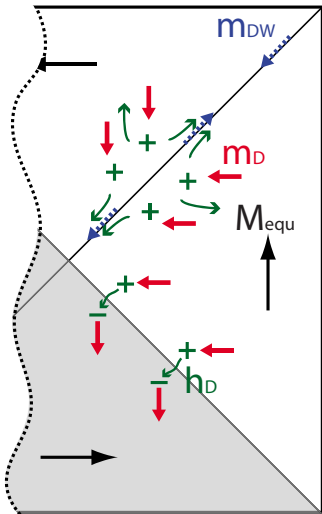


FIG. 7. (Color online) Sketch of the dynamic demagnetizing effects occurring in the vicinity of domain walls for an e_1 -type mode. The dynamic in-plane magnetization for a mostly uniform mode (m_D) is shown together with the magnetic charges and the dipole fields (h_D) it generates. The dynamic in-plane magnetization for an $n=3$ domain-wall vibration mode is also shown on the first diagonal (m_{DW}).

the dynamic magnetization of adjacent domains.^{21,22}

From a practical point of view, an excitation belonging to a given row of an irreducible representation only couples to modes belonging to the same one. For the uniform x -directed excitation field used in our case, the torque generated on the magnetization changes sign between the left and the right domain, so that it is of e_y type (see Table I). The measured absorption feature shall, therefore, be attributed to E -type modes. More precisely, we shall follow the conclusions of Sec. V, thus restricting our attention to those of the E modes which couple efficiently to a uniform excitation. In the following, we shall describe these modes using the (e_1, e_2) basis instead of the equivalent one (e_x, e_y) because the former involves a simple symmetric and/or antisymmetric behavior across each domain wall. This is shown in Fig. 7 in the case of an e_1 -type mode.

Let us first consider the behavior of this mode in the vicinity of the second diagonal ($y=-x$, see the bottom part of Fig. 7). Because the symmetry requires a change of sign for the precession angle, the dynamic magnetization adopts here a head-to-tail arrangement. This arrangement allows for an efficient compensation of the magnetic charges generated in adjacent domains, so that the mode can keep a sizable amplitude even in the vicinity of the domain wall. In such a case, the dipole field is, indeed, concentrated in the domain-wall area, where the very low value of the equilibrium effective field can compensate for it. In other words, the spin wave is strongly accelerated in the domain-wall core, allowing for a pretty abrupt change of sign for the dynamic magnetization. Compared to the isolated domain case, one, therefore, expects an increase of the amplitude of the mode in the vicinity of this domain edge (“dipolar attraction” effect). Let us now consider the vicinity of the first diagonal ($y=x$, see

the top part of Fig. 7), where the symmetry requires a head-to-head arrangement. In this case, a nonzero amplitude would generate locally very large dipole fields, which a mostly uniform mode could not accommodate. As a consequence, the amplitude is expected to vanish at this domain edge. We, therefore, end up with a symmetry-driven dipolar-dominated edge behavior: The dynamic magnetization is allowed to be large in the vicinity of the domain wall across which an antisymmetrical behavior is required, whereas it is required to be small in the vicinity of the domain-wall across which a symmetrical behavior is required. The most uniform ansatz satisfying these conditions for the right domain is obtained from Eq. (6) with $(p, q)=(1, 2)$ [see Fig. 6(b)]. To estimate the corresponding frequency, we generalize the variational estimate of Sec. V C: The Landau structure is approximated by assembling four triangular saturated domains spaced 60 nm from each other (domain walls are replaced by empty regions). The ansatz for the right domain is unfolded onto the other three domains according to the representation e_1 . The frequency is then estimated using Eq. (7), extending the space integration over the four domains and rotating properly the dynamic magnetization between them. We obtain $f_{1,2}^D=4.5$ GHz. As expected, this value is lower than the one obtained for an isolated domain, indicating that the dipolar attraction effect renormalizes significantly the mode frequencies.⁴⁸

In the description above, domain walls were assumed to be “dynamically dead,” and we have only considered their ability to accommodate for very fast magnetization changes. However, the domain wall has its own dynamics (see Sec. IV), which may interact with the domains. Indeed, an e_1 -type domain mode is expected to generate a sizable dipole field along the first diagonal, and this might couple efficiently to the dynamic magnetization of a domain-wall mode located in this region (see the top part of Fig. 7). We account for this effect with the help of a very rough perturbation approach: We calculate the dipole field generated onto the first diagonal by the domain-mode ansatz [Eq. (6) with $(p, q)=(1, 2)$] and project it over the domain-wall mode ansatz [Eq. (2) with $n=3$; this mode is, indeed, expected to couple the strongest because it is nearly degenerate with the domain modes in the range of 3–5 GHz]. After a suitable normalization, this provides a dipolar coupling factor which translates into a frequency shift $|\delta f^{D-DW}|=0.4$ GHz. The coupled system is finally expected to display two types of modes: those for which the mostly uniform domain modes and the domain-wall mode are in-phase ($f \approx f_{1,2}^D - |\delta f^{D-DW}|=4.1$ GHz) and those for which they are out of phase ($f \approx f_{1,2}^D + |\delta f^{D-DW}|=4.9$ GHz). This analysis accounts for the $D_1^0-D_1^+$ doublet observed in Fig. 2(a). Indeed, for the 4.2 GHz map of Fig. 2(b), there is no change of sign for the dynamic magnetization when reaching the domain wall (so that part of the dynamic magnetic flux generated in the domains might exit through the domain wall), whereas there is such a change of sign for the 5.2 GHz map.

Once we get a global description of both domain and domain-wall dynamics, let us summarize our interpretation of the spectra in Fig. 2(a):

(i) The peak DW_1 is attributed to the fundamental string-like vibration mode of the domain walls. The frequency of

this mode is correctly accounted for by Eq. (4) with $n=1$ [see the arrow f_1^{DW} above Fig. 2(a)]. As this frequency falls far below the manifold of domain spin waves, this mode does not extend much into the domains. Moreover, the four domain walls are far enough from each other to neglect their direct dipolar coupling.

(ii) The composite peak $DW_3-D_1^-$ is attributed to the bottom of the domain spin-wave manifold coupled to the $n_{DW}=3$ domain-wall vibration mode, with estimated frequencies $f_{min}^D=2.8$ GHz (see Sec. V B) and $f_3^{DW}-|\delta f^{D-DW}|=3.6$ GHz.

(iii) Higher frequency peaks are attributed to sets of modes selected by the uniform excitation out of a quasicontinuum of quantized domain spin waves. The composite feature $D_1^0-D_1^+$ corresponds to those of the domain modes, which are as uniform as possible. The splitting is basically associated with the coupling between these modes and the $n=3$ domain-wall vibration mode.

(iv) Features D_{2-5} are governed by the same mechanism except that the envelope functions now involve nodal lines within each domain. The amplitudes of these peaks are much lower than those of the D_1 peaks because of the smaller overlap integrals.

VII. EVOLUTION UNDER AN APPLIED FIELD

Once a global description of the dynamics of domains and domain walls is available, it becomes possible to perform true micromagnetic spectroscopy, that is, to identify a domain configuration according to its “microwave signature,” i.e., its absorption spectrum. To demonstrate this possibility, we consider in this section the spectrum measured when the sample of Fig. 1(a) is subjected to an external field H_0 directed along one diagonal of the squares [see Fig. 8(a)], and we try to deduce from it a plausible scenario for the magnetization process.

Figure 8(b) shows the quasistatic hysteresis cycle measured for a large array of dots similar to those of Fig. 1(a). Coming from a large negative field, the dot seems to remain significantly magnetized up to $\mu_0 H_0 = -2$ mT, where a low-moment state appears. Apparently, a high-moment state emerges again around 10 mT. However, the nature of these high- and low-moment configurations remains mysterious. We shall now try to elucidate this point with the help of Fig. 8(c), which shows a semilogarithmic grayscale plot of the absorption as a function of the applied field H_0 (swept from negative to positive values) and of the frequency. On such a plot, absorption features appear as clear areas in a darker background. Our understanding of the position and the shape of these absorption features is the following.

Starting at large negative values, we first distinguish several nearly parallel white trails with frequency increasing steadily as a function of $|H_0|$. This is typical of a quasisaturated configuration: The higher frequency most intense line is attributed to a set of quasiuniform modes, while the lower frequency lines are attributed to spin-wave well modes localized in the edge areas. [For comparison, see the high field spectrum of Fig. 10(b)]. Such a quasisaturated configuration is shown in Fig. 8(d), which shows the equilibrium configuration simulated after applying a -1.4 T saturating field and reducing it back to -12 mT.

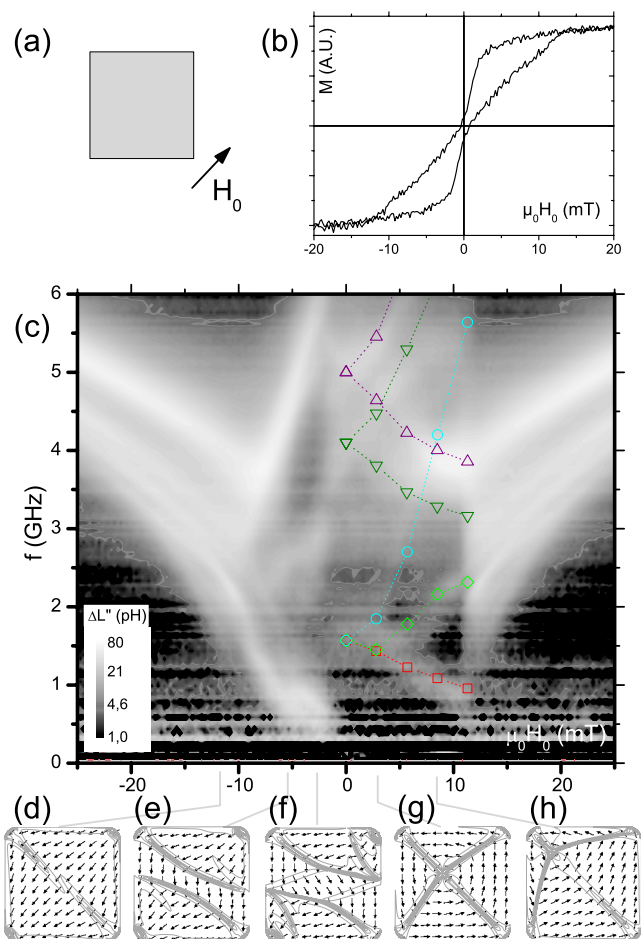


FIG. 8. (Color online) (a) Geometry for the measurement. (b) Magneto-optical Kerr effect magnetization loop measured on an array of square dots similar to those used for the microwave measurement. (c) Semilogarithmic grayscale plot of the measured absorption as a function of the external field H_0 , swept from negative to positive values, and of the frequency. The colored dots and dotted lines are deduced from calculations described in the text. [(d)–(h)] Equilibrium magnetization configuration for a few values of H_0 as indicated. The curves are the contour lines of $(\text{rot } \mathbf{M})_z$, so their concentration indicates the presence of a domain wall. The simulations were performed using the OOMMF package (Ref. 49) with the same parameters as indicated in Sec. III. The sequence (d)–(f) was obtained starting from a saturated configuration. The sequence (g) and (h) was obtained starting from the Landau state at remanence.

At -10 mT, two branches emerge from the quasisaturated spectrum at about 2 and 4 GHz, with frequency distinctly decreasing (increasing) as $|H_0|$ further decreases. We attribute this to the nucleation of a five-domain structure [see Figs. 8(e) and 8(f), which show the configurations simulated starting with the configuration of Fig. 8(d) and reducing the field to -6 and -3 mT]: The high-frequency branch is associated with the precession of the magnetization in the bottom, middle, and top domains (as $|H_0|$ decreases, the magnetization in these domains rotates parallel to their longest dimension, which causes the frequency of the most uniform modes to increase). On the other hand, the low-frequency branch is associated with the fundamental vibration modes of

the top and bottom domain walls (as $|H_0|$ decreases, these domain walls gradually decouple from the domains, resulting in a frequency decrease.) For H_0 increasing above -5 mT, this latter branch tends to zero frequency, which probably indicates that the five-domain configuration becomes less stable.

Indeed, the spectrum is seen to change abruptly at -1 mT, with the apparition of pale areas around 1.5, 4, and 5 GHz. This is reminiscent of the spectra of Fig. 2. We, therefore, postulate that a Landau configuration nucleates quite suddenly before remanence. With further increase of H_0 , the pale areas then split into several branches, showing both an increase and a decrease of f as a function of $|H_0|$. This is attributed to the field-induced deformation of the Landau state. Under a small external field, the vortex moves perpendicular to the field direction [see Figs. 8(g) and 8(h), which show the configurations simulated starting from a Landau configuration at remanence and increasing the applied field to $+3$ and $+8$ mT]. The motion of the vortex results in the narrowing (broadening) of the top and left (bottom and right) domains, resulting in an increase (decrease) of the frequency of the corresponding domain modes. These variations can be evaluated by a rough scaling: The dominating in-plane dynamic dipole field is expected to vary as $\frac{1}{w(H_0)}$, where $w(H_0)$ is the typical size of the domain. This gives $f(H_0) = f(0) \sqrt{\frac{w(0)}{w(H_0)}}$, which is plotted in Fig. 8(c) for $f(0)=4.2$ and 5 GHz (green down triangles and purple up triangles, respectively, corresponding to the two most intense peaks identified in the remanent spectrum of Fig. 2). This accounts well for the global shape of the absorption in the 3–6 GHz range. Then, the motion of the vortex also modifies the domain walls it is attached to. Under the application of a small positive field, the top-left, bottom-right, and two remaining domain walls get respectively strongly shortened, strongly elongated, and weakly elongated [see Fig. 8(g)], which should directly affect the corresponding vibration modes. The $n=1$ domain-wall mode peak observed at 1.5 GHz at remanence is, therefore, expected to split into three branches. The frequencies of these features can be estimated with the help of the variational approach described in Sec. IV, in which the domain-wall length and width extracted from equilibrium simulations are injected. The results of this calculation, shown in Fig. 8(c) as green diamonds, cyan circles, and red squares (corresponding respectively to the bottom-right, top-left, and two remaining domain walls), account quite well for the observed absorption. The inflection of the line joining the green diamonds, which may appear surprising at first glance, is actually a direct manifestation of the field expulsion-penetration phenomenon:⁵⁰ For very low H_0 , the domain configuration distorts itself in order to produce a dipole field which exactly cancels the applied field. However, this becomes too difficult when H_0 becomes too high. As a consequence, the external field penetrates in the element along the first diagonal, resulting in the shortening of the bottom-right domain wall [see Fig. 8(h)], i.e., in the increase of the associated vibration frequency.

Another abrupt change is finally observed at $\mu_0 H_0 = 11$ mT, corresponding to the reappearance of the quasisaturated configuration as suggested by the parallel pale trails which are observed again.

In summary, the measured absorption spectrum is properly accounted for by the magnetization process scenario sketched in Figs. 8(d)–8(h). Note that this scenario differs from the one provided by a direct micromagnetic simulation of the magnetization process, which indicates the survival of the high-moment five-domain configuration up to a quite strong positive field (not shown). Our scenario, involving the nucleation of the low-moment Landau state before remanence, is certainly in better agreement with the measured hysteresis loop. Note also that this spectroscopic technique provides quite local information in spite of its spatially averaged character. For instance, the field penetration phenomenon evidenced above is quite a subtle one, and high resolution–high sensitivity imaging would have been required for its direct observation in real space.

VIII. CONCLUSION

In this paper, we have proposed a semianalytical description for both domain and domain-wall modes in the case of a Landau equilibrium configuration. The generic ingredients for this description are the following. A domain wall should be seen as a specific micromagnetic object having a sizable influence on spin waves. On one hand, it confines low-frequency spin waves, thus creating highly localized modes which can be seen as simple stringlike vibration modes. On the other hand, it scatters the higher frequency spin waves propagating through the domains, which sets the geometry for the quantization process. Those of the quantized domain modes which couple efficiently to the excitation and/or detection signals than give rise to measurable absorption features. Due to the complicated shape of the dipole-exchange dispersion, the quantization process for spin waves becomes quite complicated as long as the geometry is not highly regular (which is the case for the triangular domains forming the Landau configuration). The absorption might then be distributed over a large set of modes rather than concentrated into a few individual modes. The frequency of the corresponding features is also influenced by dynamic interdomain couplings, which strongly depend on the global symmetry of the eigenmode considered. Accounting for these specific effects, we could unambiguously identify and interpret the absorption features observed in Fig. 2. This result, which constitutes the main achievement of this paper, opens the attractive perspective of a true micromagnetic spectroscopy.

ACKNOWLEDGMENTS

The authors wish to thank S. O. Demokritov and B. Hillbrands for providing the Permalloy film, and O. Giraud for useful discussions. M.B. acknowledges the support from the Ecole Polytechnique and from the priority program SPP1133 “Ultrafast magnetization processes” of the Deutsche Forschungsgemeinschaft.

APPENDIX: REGULAR AND IRREGULAR SPIN-WAVE SPECTRA

As already mentioned in Sec. V, the global appearance of a confined spin-wave spectrum depends quite drastically on

the amount of symmetry of the confining body. The aim of this appendix is to make this rather vague assertion more precise with the help of an analogy. For this purpose, we first quote some results on the regularity of the motion in billiard systems. We then show how to identify qualitatively a spin-wave problem to a classical billiard one. Finally, we provide an experimental illustration of the relevance of the notion of regularity for spin-wave spectra.

1. Classical billiards and wave billiards

In the classical planar billiard problem, one considers a pointlike particle moving freely within a two-dimensional enclosure and undergoing specular reflections at the boundary of this enclosure. The hard-wall reflection condition makes this problem nonlinear, and the motion is generally chaotic.⁵¹ However, for a few special geometries, the problem is said to be “integrable,”⁵² which basically means that there exists an extra constant of motion besides the energy. This restricts the motion in phase space to a two-dimensional torus, and the resulting trajectories have a highly regular appearance [see Fig. 9(a)]. The only geometries for which the classical billiard problem is integrable are the rectangles, the ellipses, and several special polygons.⁵¹ The integrability of rectangular and elliptical billiards can be seen as a simple consequence of their separability. A separation of variables in the Hamilton-Jacobi equation reduces, indeed, the problem to two one-dimensional problems which are automatically integrable (in one dimension, only one constant of motion—the energy—is required). On the other hand, for the generic nonintegrable case [see Fig. 9(b)], the motion explores the whole three-dimensional constant energy surface of the phase space (ergodicity) and the resulting trajectories look highly irregular. As a matter of fact, generic polygonal billiards (i.e., having one angle not rationally related to π) are also nonintegrable, because the surface restricting the motion in phase space is infinitely handled, resulting in an ergodic motion.⁵¹

The wave billiard problem (also called quantum billiard) consists in the determination of the spectrum of a particle confined in a two-dimensional enclosure with hard walls. It has naturally a deep connection with its classical counterpart: only in the classically integrable systems is a simple quantization procedure available. In particular, separable problems are easily quantized because the wave equation reduces to two one-dimensional wave equations which can be solved separately. The quantum numbers provided by such a procedure allow one to classify the wave functions and to build selection rules (i.e., to predict which wave functions are likely to couple to a well-defined excitation), which are of great importance in practice. Figure 9(d) shows the qualitative features of the absorption spectrum for a rectangular wave billiard subjected to a uniform excitation. The standing-wave indices (n_x, n_y) , which constitute the relevant quantum numbers in that case, are used for labeling the normal modes and for predicting the magnitude of their coupling to the excitation (the coupling is inversely proportional to $n_x^2 n_y^2$ for both n_x and n_y odd, and zero otherwise). The wave functions look quite regular, with two arrays of nodal

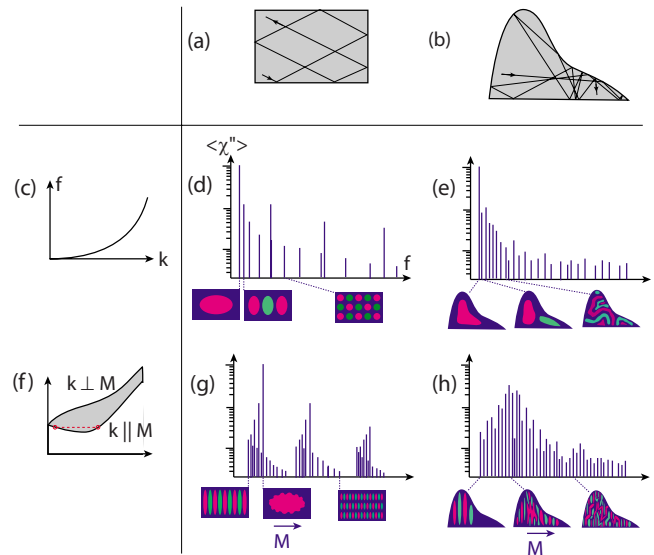


FIG. 9. (Color online) Schematic representation of the analogy between classical billiards, wave billiards, and quantized spin-wave problems. (a) Typical example for an integrable classical billiard; a typical trajectory is also shown. (b) Same for a nonintegrable classical billiard. (c) Typical wave dispersion (e.g., that of a free quantum particle wave). (d) Sketch of the spectrum for a wave billiard in the integrable case [the shape of the enclosure is the same as in (a)]. The height of the vertical bars is proportional to the squared average of the wave function (so that it describes the coupling to a uniform excitation). Three wave functions are also sketched [color scale as in Fig. 2(b)]. (e) Same for the nonintegrable case. (f) Wave dispersion for spin waves in an in-plane magnetized film. (g) Sketch of a “regular” spin-wave spectrum (i.e., the shape of the magnetic body corresponds to an integrable classical billiard). (h) Sketch of an “irregular” spin-wave spectrum.

lines oriented perpendicular to each other. On the other hand, there is no such simple quantization procedure in the nonintegrable case. This means that the only index available for classifying the solutions is their energy ordering. This also means that there are no selection rules, so that every mode could *a priori* couple to a uniform excitation. Let us mention another result which constitutes a basis of the common intuition one has on wave problems. In standard wave mechanics, one encounters positive wave dispersions [i.e., the frequency increases as the wave vector increases, see Fig. 9(c)]. Then, for confined geometries, the magnitude of the wave vector is estimated by counting nodal domains. So it is generally admitted that the mode frequency increases steadily as the number of nodal domains increases (a result known as Chladni’s rule or Courant nodal line count theorem).⁴⁴ This rule enables generic predictions about the appearance of the low lying wave functions (first mode as uniform as possible, second one containing one nodal line roughly in the middle of the body, etc.) and their coupling to, e.g., a uniform excitation. On the other hand, the higher order wave functions for nonintegrable billiards are expected to look quite chaotic, with meanderlike nodal domains.^{51,53} In semiclassical terms, these wave functions take their complexity from the classical trajectories they are built onto. Figure 9(e) shows qualita-

tively these features for a generic wave billiard in the non-integrable case.

2. Spin-wave billiards

The determination of the spin-wave modes in a thin magnetic element constitutes a wave-mechanics problem, which is formally analogous to the wave billiard.⁵⁴ However, there are several essential differences which are made apparent by looking at the respective wave dispersions. In contrast with the simple parabolic dispersion of quantum mechanics [Fig. 9(c)], the dipole-exchange dispersion for a spin wave propagating in an in-plane magnetized film is, indeed, both anisotropic (with respect to the angle between the wave vector and the equilibrium magnetization) and nonmonotonic [Fig. 9(f)].^{2,29}

Qualitatively, an anisotropic wave problem can be mapped over an isotropic one by simply rescaling one axis compared to the other. A confined spin-wave problem should, therefore, be identified to a classical billiard whose shape is deduced from that of the “spin-wave billiard” by an elongation along the direction of the equilibrium magnetization. For example, rectangular bodies magnetized along one edge are expected to have a regular spectra (because the equivalent classical billiard is also rectangular, i.e., integrable; note that this problem is even close to separable). However, the appearance of this regular spectra is largely influenced by the nonmonotonic shape of the spin-wave dispersion: because the frequency may decrease as the wave vector increases, the Chladni rule is broken and some high-index low-intensity modes are brought below the low-index high-intensity ones [Fig. 9(g)]. In addition, for a certain range of frequencies, one may have two different wave-vectors at the same frequency [see dotted line in Fig. 9(f)]. A wave can, therefore, split into two waves after reflection on the boundary. This leads to a certain mixing of the short- and long- wavelength spin waves, which may give a rippled appearance to some modes [see Fig. 9(g)].

Figure 9(h) shows a typical irregular spin-wave spectrum, expected when the classical billiard obtained after the rescaling operation is not integrable. Compared to Fig. 9(e), the complexity of the spectrum is still increased because the degree of uniformity of one mode is not simply related to its frequency anymore.

3. Experimental check: Spin-wave spectrum in an obliquely saturated square dot

To illustrate the fundamental difference between regular and irregular spin-wave spectra, we shall now compare results obtained for the same physical system (a quasisaturated square dot), which can be made to have either a regular spectra (when the external field is applied along one edge) or an irregular one (when the external field is applied along one diagonal).

The spectra reported in Fig. 10(a) are the same as those of Fig. 6(c) of Ref. 4. The experimental spectrum was obtained using the same micrometer square Permalloy dots as those used in the present paper and applying a 80 mT quasisatu-

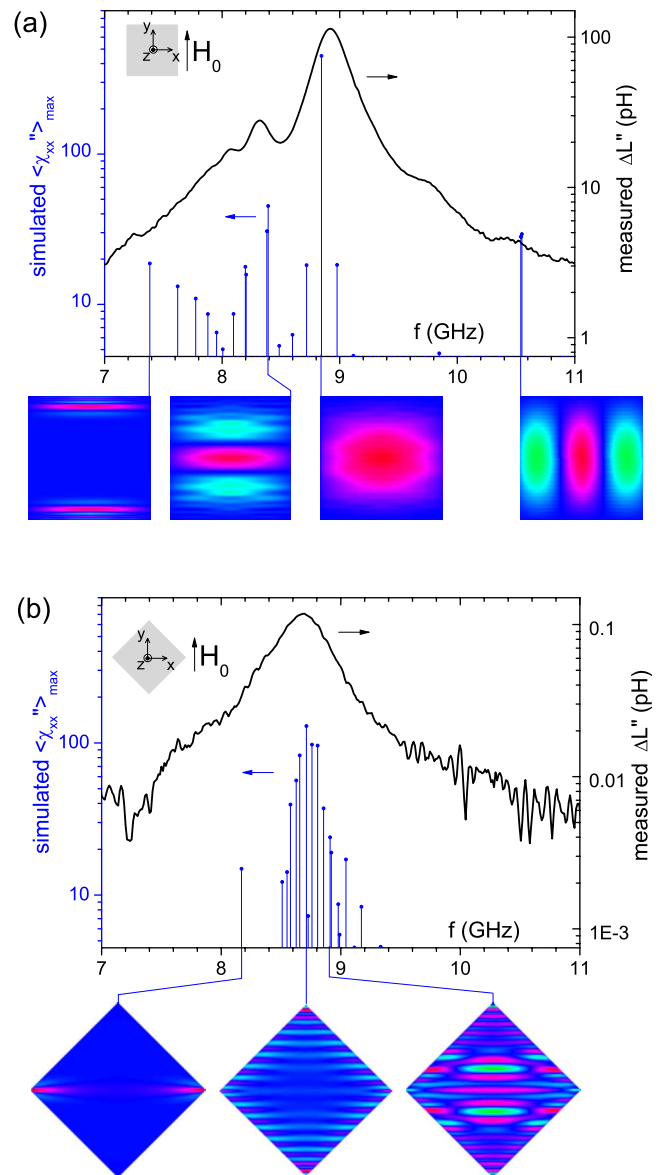


FIG. 10. (Color online) Comparison of regular and irregular spin-wave spectra. (a) Measured and calculated spectra for Permalloy square dots subjected to an in-plane quasisaturating field $\mu_0 H_0 = 80$ mT directed along one side of the squares. The measured spectrum (black curve) has been obtained using the broadband inductive technique described in the text. The calculated spectrum (vertical blue bars) has been obtained by a diagonalization of the dynamical matrix. The maps of a few selected eigenmodes are also shown. (b) Same for the in-plane quasisaturating field directed along one diagonal of the square.

rating external field along one edge of the dots. The vertical bars are the result of a diagonalization procedure similar to that of Sec. V. As foreseen in the last section, the absorption for this regular system is concentrated in several well-resolved peaks, each of them being associated with a single eigenmode.

Let us now turn our attention to the spectra reported in Fig. 10(b), for which the 80 mT external field was oriented along one diagonal of the dots. The spin-wave spectrum is

now expected to be irregular: after elongation along one of its diagonal, a square becomes, indeed, a flat rhombus, and rhombus billiards are generally not integrable. Indeed, the measured absorption [see black line in Fig. 10(b)] is somewhat spread over a single wide peak. The diagonalization [see vertical bars in Fig. 10(b)] shows that this peak consists of several modes whose frequency spacing is smaller than the intrinsic linewidth of the Permalloy film, so that they cannot be resolved experimentally. It should be noted that these results are in good agreement with those of Barman *et al.*,⁵⁵ who measured the transient magnetization distribution in a square dot and observed a much more irregular behavior when the field was applied along the diagonal of the square. In a similar way, the domain mode spectra studied in this paper belong to the class of irregular spectra. Indeed, the domains of the Landau configuration have the shape of isorectangle triangles. After elongation along the direction of the equilibrium magnetization, these triangles become generic isosceles ones, and classical billiards with generic triangular shape are not integrable.

To conclude, let us summarize the mechanisms responsible for the relatively featureless spin-wave spectra obtained

for saturated bodies with generic polygonal shapes: Generic polygonal geometries are ergodic, so that the motion explores the whole isofrequency line in the wave-vector space. Due to the complex anisotropic and nonmonotonic shape of the dipole-exchange dispersion, this isofrequency line covers, in general, a wide range of wave vectors, from very long to very short wavelengths. As a consequence, the modes cannot be described by well-defined quantization wave vectors (except the lowest frequency mode which lies at the minimum of the spin-wave dispersion). In particular, one cannot define a quasiuniform mode, because the longest wavelength spin wave is continuously scattered over all the degenerate spin waves. Indeed, the main absorption peak for a uniform excitation is composed of several modes whose y profiles display both a slowly varying background and a fast oscillating component [see the 4.7, 5.1, and 5.4 GHz maps in Fig. 4 or the 8.7 and 8.9 GHz maps in Fig. 10(b)]. This is in contrast with, e.g., rectangular bodies magnetized along one side, for which the reflections on the sides give only access to a small number of wave-vector values (integrable dynamics), so that a well-defined quantization wave vector can be assigned to each mode.

*bailleul@ipcms.u-strasbg.fr

- ¹B. Hillebrands, K. Ounadjela, and A. E. Thiaville, *Spin Dynamics in Confined Magnetic Structures* (Springer, Berlin, 2001), Vol. 1; *ibid.* (Springer, Berlin, 2001), Vol. 2.
- ²B. A. Kalinikos and A. N. Slavin, *ibid.* **19**, 7013 (1986).
- ³M. Buess, T. P. J. Knowles, R. Höllinger, T. Haug, U. Krey, D. Weiss, D. Pescia, M. R. Scheinfein, and C. H. Back, *Phys. Rev. B* **71**, 104415 (2005).
- ⁴M. Bailleul, R. Höllinger, and C. Fermon, *Phys. Rev. B* **73**, 104424 (2006).
- ⁵L. Giovannini, F. Montoncello, F. Nizzoli, G. Gubbiotti, G. Carlotti, T. Okuno, T. Shinjo, and M. Grimsditch, *Phys. Rev. B* **70**, 172404 (2004).
- ⁶G. Gubbiotti, G. Carlotti, T. Okuno, M. Grimsditch, L. Giovannini, F. Montoncello, and F. Nizzoli, *Phys. Rev. B* **72**, 184419 (2005).
- ⁷K. E. Buchanan, P. E. Roy, M. Grimsditch, F. Y. Fradin, K. Y. Guslienko, S. D. Bader, and V. Novosad, *Nat. Phys.* **1**, 172 (2005).
- ⁸I. Neudecker, K. Perzlmaier, F. Hoffmann, G. Woltersdorf, M. Buess, D. Weiss, and C. H. Back, *Phys. Rev. B* **73**, 134426 (2006).
- ⁹R. Hertel, W. Wulfhekel, and J. Kirschner, *Phys. Rev. Lett.* **93**, 257202 (2004).
- ¹⁰C. Bayer, H. Schultheiss, B. Hillebrands, and R. L. Stamps, *IEEE Trans. Magn.* **41**, 3094 (2005).
- ¹¹J. P. Park, P. Eames, D. M. Engebretson, J. Berezovsky, and P. A. Crowell, *Phys. Rev. B* **67**, 020403(R) (2003).
- ¹²S. B. Choe, Y. Acremann, A. Scholl, A. Bauer, A. Doran, J. Stöhr, and H. A. Padmore, *Science* **304**, 420 (2004).
- ¹³H. Stoll, A. Puzic, B. van Waeyenberge, P. Fisher, J. Raabe, M. Buess, T. Haug, R. Höllinger, C. Back, D. Weiss, and G. Denbeaux, *Appl. Phys. Lett.* **84**, 3328 (2004).
- ¹⁴K. Perzlmaier, M. Buess, C. H. Back, V. E. Demidov, B. Hill-

- ebands, and S. O. Demokritov, *Phys. Rev. Lett.* **94**, 057202 (2005).
- ¹⁵J. Raabe, C. Quitmann, C. H. Back, F. Nolting, S. Johnson, and C. Buehler, *Phys. Rev. Lett.* **94**, 217204 (2005).
- ¹⁶A. Krasnyuk, F. Wegelin, S. A. Nepijko, H. J. Elmers, G. Schonenhense, M. Bolte, and C. M. Schneider, *Phys. Rev. Lett.* **95**, 207201 (2005).
- ¹⁷M. Buess, J. Raabe, K. Perzlmaier, C. H. Back, and C. Quitmann, *Phys. Rev. B* **74**, 100404(R) (2006).
- ¹⁸K. W. Chou, A. Puzic, H. Stoll, D. Dolgos, G. Schtz, B. Van Waeyenberge, A. Vansteenkiste, T. Tylliszczak, G. Woltersdorf, and C. H. Back, *Appl. Phys. Lett.* **90**, 202505 (2007).
- ¹⁹The Landau configuration comprises four domains separated by four 90° domain walls and one vortex. It is the most stable remanent state for large enough square element.
- ²⁰C. Vaast-Paci and L. Leylejian, *J. Magn. Magn. Mater.* **237**, 342 (2001).
- ²¹M. Yan, G. Leaf, H. Kaper, R. Camley, and M. Grimsditch, *Phys. Rev. B* **73**, 014425 (2006).
- ²²M. Bolte, G. Meier, and C. Bayer, *Phys. Rev. B* **73**, 052406 (2006).
- ²³A. Kaya and A. J. Bain, *J. Appl. Phys.* **99**, 08B708 (2006).
- ²⁴K. Rivkin and J. B. Ketterson, *J. Magn. Magn. Mater.* **306**, 204 (2006).
- ²⁵In this case, the reference data had been taken in a field of 45 mT applied perpendicular to the axis of the coplanar waveguide, which also sets the magnetic history of the sample. Measurements in the quasaturated state have shown that the absorption is very low for this direction of the field (Ref. 4), which ensures that our reference is a correct one.
- ²⁶<http://llgmicro.home.mindspring.com>
- ²⁷Note also that the vortex translation mode does not appear in Fig. 2. This is because its frequency is far below the range investi-

- gated here [it is expected in the 100 MHz range for the dimensions of our dots (Ref. 56)].
- ²⁸More precisely, the total absorption at frequency f can be written as a sum over all normal modes (Ref. 24), each normal mode being weighted by a factor containing the Lorentzian $1/[(f - f_n)^2 + \delta f_n^2]$, where f_n and δf_n are respectively the frequency and linewidth of mode n (see, e.g., Appendix B of Ref. 4 for a derivation of this factor).
- ²⁹R. W. Damon and J. R. Eshbach, *J. Phys. Chem. Solids* **19**, 308 (1961).
- ³⁰A. Hubert and R. Schäfer, *Magnetic Domains* (Springer, Berlin, 1998).
- ³¹H. Riedel and A. Seeger, *Phys. Status Solidi B* **46**, 377 (1971).
- ³²J. Jorzick, S. O. Demokritov, B. Hillebrands, M. Bailleul, C. Fermion, K. Y. Guslienko, A. N. Slavin, D. V. Berkov, and N. L. Gorn, *Phys. Rev. Lett.* **88**, 047204 (2002).
- ³³A. P. Malozemoff and J. C. Slonczewski, *Magnetic Domain Walls in Bubble Materials* (Academic, New York, 1979).
- ³⁴M. Ramesh and P. E. Wigen, *J. Magn. Magn. Mater.* **74**, 123 (1988).
- ³⁵The vortex is assumed to be dynamically “dead” for the range of frequencies investigated here (Ref. 56).
- ³⁶M. Sparks, *Phys. Rev. B* **1**, 3831 (1970).
- ³⁷K. Y. Guslienko and A. N. Slavin, *J. Magn. Magn. Mater.* **215-216**, 576 (2000).
- ³⁸R. Zivieri and R. L. Stamps, *Phys. Rev. B* **73**, 144422 (2006).
- ³⁹We also performed a full spin-wave calculation (not shown), which describes how the H_{equ} profile shown in Fig. 3(b) generates localized spin-wave modes and how the dipole-exchange equilibrium and dynamic fields combine to set the mode frequencies. This calculation basically confirms the result of the much simpler domain-wall resonance approach. In addition, it indicates that the H_{equ} well is not deep enough to admit a second bound state. (Such a mode would have one nodal line along the wall core, thus corresponding to a “breathing” of the domain-wall core.)
- ⁴⁰The assumption of a uniform equilibrium magnetization distribution is quite a crude one, but we believe that the conclusions of this study are robust because the modes obtained are mostly located in the saturated interior part of the domain, so they are not expected to be strongly influenced by the exact equilibrium magnetic configuration at the edges.
- ⁴¹In all the diagonalization and variational calculations relative to domain modes, we assume $h_z = -m_z$ (which corresponds to the long-wavelength hypothesis of Appendix A in Ref. 4). This is justified by the fact that the spin-wave dispersions are only weakly affected by this assumption when the equilibrium field is low enough. This simplification allows one to restrict the diagonalization to one block of the full dynamical matrix [block D_x in Eq. (12) of Ref. 4]. As this block is symmetrical, one can use a quite efficient symmetrical matrix diagonalization routine. We also neglect in our calculations the equilibrium field H_{equ} . Indeed, H_{equ} is low and quite uniform except in the domain-wall core [see Fig. 3(b)]. Taking it into account would result in a slight negative shift for all mode frequencies.
- ⁴²W. H. Press, S. A. Teukolsky, W. T. Vetterling, and B. P. Flannery, *Numerical Recipes in C* (Cambridge University Press, Cambridge, England, 1992).
- ⁴³K. Y. Guslienko and A. N. Slavin, *Phys. Rev. B* **72**, 014463 (2005).
- ⁴⁴R. Courant and D. Hilbert, *Methods of Mathematical Physics* (Interscience, New York, 1953), Vol. 1.
- ⁴⁵Note that the functions of Eq. (6) would actually be true eigenmodes for the quantized wave problem if the wave dispersion were isotropic [the isorectangle triangular classical billiard is known to be integrable (Ref. 51)]. This is not true for any anisotropic wave dispersion, because the two terms of Eq. (6) now correspond to different angles for the quantization wave vectors.
- ⁴⁶R. S. Knox and A. Gold, *Symmetry in the Solid State* (Benjamin, New York, 1964).
- ⁴⁷ C_{4v} is the relevant symmetry group in our case because we neglect the vortex (Ref. 21).
- ⁴⁸We also performed a full diagonalization calculation in this geometry (not shown). This confirmed the role of the symmetry in determining the edge behavior of the modes. In particular, we could reproduce the dipolar attraction effect mentioned above for E -type modes.
- ⁴⁹*Object Oriented Micro Magnetic Framework*, www.nist.gov
- ⁵⁰R. Schäfer and A. DeSimone, *IEEE Trans. Magn.* **38**, 2391 (2002).
- ⁵¹M. Berry, in *Chaotic Behaviour of Deterministic Systems*, edited by G. Iooss, R. H. G. Helleman, and R. Stora (North Holland, Amsterdam, 1983), pp. 171–272.
- ⁵²V. I. Arnol’d, *Mathematical Methods of Classical Mechanics* (Springer, New York, 1978).
- ⁵³M. G. Gutzwiller, *Chaos in Classical and Quantum Mechanics* (Springer, New York, 1990).
- ⁵⁴In this appendix, we do not discuss the influence of the long-range character of the dipolar interaction nor that of the strongly inhomogeneous magnetic configurations. For the global description of the spectrum of a quasisaturated magnetic body, we believe that the most relevant properties of the dipole-exchange operator are included in the spin-wave dispersion.
- ⁵⁵A. Barman, V. V. Kruglyak, R. J. Hicken, J. M. Rowe, A. Kundrotaite, J. Scott, and M. Rahman, *Phys. Rev. B* **69**, 174426 (2004).
- ⁵⁶K. Y. Guslienko, X. F. Han, D. J. Keavney, R. Divan, and S. D. Bader, *Phys. Rev. Lett.* **96**, 067205 (2006).